

Secrecy Performance Analysis of Multi-Functional RIS-Assisted NOMA Networks

Yingjie Pei, *Graduate Student Member, IEEE*, Wanli Ni, *Member, IEEE*, Jin Xu, *Member, IEEE*, Xinwei Yue, *Senior Member, IEEE*, Xiaofeng Tao, *Senior Member, IEEE*, and Dusit Niyato, *Fellow, IEEE*

Abstract—Although reconfigurable intelligent surface (RIS) can improve the secrecy communication performance of wireless users, it still faces challenges such as limited coverage and double-fading effect. To address these issues, in this paper, we utilize a novel multi-functional RIS (MF-RIS) to enhance the secrecy performance of wireless users, and investigate the physical layer secrecy problem in non-orthogonal multiple access (NOMA) networks. Specifically, we derive closed-form expressions for the secrecy outage probability (SOP) and secrecy throughput of users in the MF-RIS-assisted NOMA networks with external and internal eavesdroppers. The asymptotic expressions for SOP and secrecy diversity order are also analyzed under high signal-to-noise ratio (SNR) conditions. Additionally, we examine the impact of receiver hardware limitations and error transmission-induced imperfect successive interference cancellation (SIC) on the secrecy performance. Numerical results indicate that: i) under the same power budget, the secrecy performance achieved by MF-RIS significantly outperforms active RIS and simultaneously transmitting and reflecting RIS; ii) with increasing power budget, residual interference caused by imperfect SIC surpasses thermal noise as the primary factor affecting secrecy capacity; and iii) deploying additional elements at the MF-RIS brings significant secrecy enhancements for the external eavesdropping scenario, in contrast to the internal eavesdropping case.

Index terms— Multi-functional reconfigurable intelligent surface, non-orthogonal multiple access, outage probability, physical layer secrecy, performance analysis.

I. INTRODUCTION

Future sixth-generation (6G) networks need to satisfy the demands for greater bandwidth, higher speeds, and lower latency [1], [2]. This necessitates trends towards higher radio frequencies and larger antenna arrays in 6G networks [3]. Reconfigurable intelligent surface (RIS), as a two-dimensional implementation of electromagnetic metamaterials, intelligently regulate spatial electromagnetic waves with controllable amplitude, phase, and frequency in a programmable manner [4],

This work was supported by National Natural Science Foundation of China under Grant 61932005. (*Corresponding author: Xiaofeng Tao.*)

Y. Pei, J. Xu and X. Tao are with the School of Information and Communication Engineering, Beijing University of Posts and Telecommunications, Beijing 100876, China (email: yingjie.pei@bupt.edu.cn, jin.xu@bupt.edu.cn, taoxf@bupt.edu.cn).

W. Ni is with the Department of Electronic Engineering, Tsinghua University, Beijing 100084, China, and also with the Beijing National Research Center for Information Science and Technology, Beijing 100084, China (email: niwanli@tsinghua.edu.cn).

X. Yue is with the Key Laboratory of Information and Communication Systems, Ministry of Information Industry and also with the Key Laboratory of Modern Measurement & Control Technology, Ministry of Education, Beijing Information Science and Technology University, Beijing 102206, China (email: xinwei.yue@bistu.edu.cn).

D. Niyato is with the College of Computing and Data Science, Nanyang Technological University, Singapore 639798 (email: dniyato@ntu.edu.sg).

[5]. RIS has emerged as one of the highly anticipated candidate technologies for 6G in recent years [6]. Prior studies have demonstrated that deploying RIS can significantly enhance the coverage and capacity of wireless communication networks [7], [8], enable facilitate sensing and localization [9], [10], and guarantee secure communication at the physical layer [11], [12], [13].

One of the main limitations of traditional RIS is its ability to serve users only in a half-space [14]. To overcome this issue, the simultaneously transmitting and reflecting RIS (STAR-RIS) with dual functionality was proposed in [15]. Generally, STAR-RIS can control the magnitude and phase of incoming signals by adjusting the bias voltage at the embedded PIN diode, enabling signal propagation on both sides of the surface [16]. The authors in [17] proposed three typical operating modes of STAR-RIS, namely energy splitting (ES), mode switching, and time switching. The authors of [18] studied the coverage characteristics of STAR-RIS-assisted massive antenna networks. By redesigning the transmission and reflection coefficients, STAR-RIS can provide communication networks with superior secrecy rate compared to RIS schemes [19]. Furthermore, an active monitoring system assisted by STAR-RIS was proposed in [20], where STAR-RIS can enhance the eavesdropping performance of the monitor while ensuring its concealment.

Additionally, the excellent adaptability of STAR-RIS allows it to integrate with emerging multiple access technologies, such as non-orthogonal multiple access (NOMA), achieving mutual benefits [21]. The core idea of the NOMA technology is to differentiate users in the power domain to achieve ultra-high spectrum efficiency [22]. The authors in [23] studied the rate performance STAR-RIS-assisted NOMA networks, deriving closed-form and approximate expressions for ergodic rate. Furthermore, authors in [24] analyzed the outage behavior and throughput of users in STAR-RIS-assisted NOMA networks. The error characteristics of NOMA networks were explored via STAR-RIS in [25], deriving closed-form solutions for block error rate and goodput. The authors in [26] proposed a scaling and rotating constellations method to match the optimal parameters of STAR-RIS, thereby improving the error-rate performance of uplink NOMA networks.

Although the collaboration between STAR-RIS and NOMA networks holds a prospective future, the full-space coverage transmission facilitated by STAR-RIS in NOMA networks exacerbates the risk of eavesdropping on users' private signals. For this issue, the secrecy performance of STAR-RIS-assisted NOMA networks was investigated in [27], where

both closed-form and approximate expressions of secrecy rate were derived. The authors of [28] considered the impact of residual hardware impairments at the transceiver on the outage behavior of private signals in STAR-RIS-secured NOMA networks. The secrecy rate of NOMA networks was maximized in [29] with the assistance of artificial noise at the base station (BS) and the beamforming design at STAR-RIS. The aforementioned literatures only consider the external eavesdropping case. However, users located within the service area have the opportunity to wiretap others' information, making them internal Eves (I-Eves). The authors in [30] proposed a STAR-RIS-secured NOMA networks with the presence of an I-Eve, where the coefficients at STAR-RIS are adjusted to maximize the secure rate of users. Building upon this, the secrecy capacity of uplink NOMA networks was optimized in [31] with discrete phase-shifted STAR-RIS. Furthermore, the authors in [32] enhanced the capability of STAR-RIS in guaranteeing the secrecy rate and outage behavior of NOMA networks by devising appropriate power allocation and user pairing strategies under both external and internal eavesdropping scenarios.

Another constraint on the deployment of STAR-RIS-assisted NOMA networks is that introducing STAR-RIS can lead to signal degradation due to the existence of multiplicative fading [33], [34]. In response to the issue, a novel multi-functional RIS (MF-RIS) was recently proposed in [35], embedding with low-cost and power-controllable amplifiers to ensure signal propagation in full space while mitigating the influence of multiplicative fading. The outage behaviors and ergodic rate of MF-RIS over STAR-RIS were evaluated in [36], where MF-RIS exhibits a lower outage probability with a small number of elements. The authors in [37] validated that by redesigning the reflection and refraction parameters, the throughput of MF-RIS networks exceeds both STAR-RIS and traditional RIS. The sum-rate optimization of MF-RIS-enhanced uplink networks was investigated in [38] by redesigning the transmitting power and the received beamforming vector. The authors in [39] comprehensively studied the sum-rate performance of MF-RIS-assisted NOMA networks. As a further advance, the authors in [40] surveyed the potential of MF-RIS in enhancing the sum-rate performance of massive multiple-input multiple-output networks over correlated fading channels.

A. Motivations

The aforementioned literature emphasizes the crucial role played by the MF-RIS in boosting user throughput in NOMA networks, mitigating outage probability, and minimizing energy consumption. Nevertheless, by amplifying the confidential signals across the entire space, MF-RIS also exposes vulnerabilities to malicious Eves [19]. Furthermore, the impact of thermal noise generated by active components in MF-RIS on secure signal transmission remains unknown, which has never been considered in traditional RIS and STAR-RIS assisted networks [13], [33]. The work in [27] analyzed the secrecy performance of STAR-RIS-assisted NOMA networks but only considered the external eavesdropping scenario. In addition, the work in [29] - [32] surveyed the secrecy characteristics

of STAR-RIS-assisted NOMA networks from an optimization design perspective, lacking theoretical analysis. In this paper, we aim to explore the potential capabilities of MF-RIS in safeguarding NOMA networks by seeking answers to these questions.

- How does the significant thermal noise generated by the active components in MF-RIS affect the network's secrecy communications?
- When comparing imperfect successive interference cancellation (SIC) with thermal noise, which factor poses a greater risk to the secrecy performance of MF-RIS-assisted NOMA networks?
- What are the disparities in the secrecy performance of MF-RIS-assisted NOMA networks across various eavesdropping scenarios?

B. Contributions

To the best of our knowledge, this paper presents the first comprehensive analysis of the physical layer secrecy performance of MF-RIS-assisted NOMA networks. Specifically, we delve into the secure communication capabilities of randomly distributed users within these networks, taking into account both external and internal eavesdropping threats. Additionally, we derive closed-form and asymptotic expressions of the secrecy outage probability (SOP) of users, considering both imperfect and perfect SIC scenarios. Furthermore, we evaluate the impact of various factors, including the total power budget, the number of reconfigurable elements, residual interference, and thermal noise, on the secure communication in MF-RIS-assisted NOMA networks. The major contributions of this paper can be summarized as follows:

- 1) We propose an MF-RIS-secured NOMA network, leveraging the MF-RIS to enhance the quality of legitimate cascaded channels through coherent phase shifting. To extensively evaluate the secrecy performance, we consider both external and internal wiretapping scenarios. Additionally, we select the SOP of randomly distributed users as the key metric to demonstrate the superior secrecy capabilities of MF-RIS compared to STAR-RIS and active RIS schemes.
- 2) For the external wiretapping scenarios, an illegal external Eve (E-Eve) attempts to intercept the private messages of users served by the MF-RIS. Firstly, we examine the characteristics of the wiretapped cascaded channels. Taking into account the hardware limitations at receivers, we then derive closed-form expressions of the SOP and secrecy throughput of both users, considering both imperfect and perfect SIC cases. To gain further insights, we also obtain asymptotic SOP expressions as the transmit power approaches infinity. Then, we obtain the secrecy diversity order, which is proportional to the number of MF-RIS elements.
- 3) For the internal wiretapping scenarios, the user positioned within the reflection region and enjoying superior channel conditions is designated as the I-Eve. This user is capable of decoding the private information transmitted to the user on the opposite side. Given that the I-Eve

is a legitimate and registered user, their cascaded channels can be enhanced through the coherent phase shifting capabilities of the MF-RIS. To address this issue, we re-examine the characteristics of the wiretapping channels and derive the SOP expressions of the user located in the refraction region, considering both imperfect and perfect SIC cases. However, due to the presence of imperfect SIC and the I-Eve, the secrecy diversity order of the other users on the opposite side consistently remains at zero.

- 4) Numerical results confirm the precision of our theoretical analyses and further highlight several key findings: Firstly, within the same power budget, MF-RIS-secured NOMA networks outperform both STAR-RIS and active RIS-based schemes in terms of SOP and secrecy throughput. Secondly, while an increase in the number of MF-RIS elements significantly enhances user secrecy in external eavesdropping scenarios, its impact may be limited in internal eavesdropping scenarios due to the I-Eve's ability to benefit from the same diversity gain. Finally, both thermal noise at the MF-RIS and residual interference resulting from imperfect SIC affect private signal transmission, with the latter gradually emerging as the primary factor as the power budget increases.

II. SYSTEM MODEL

A. Network Descriptions

We consider an MF-RIS-secured NOMA network as illustrated in Fig. 1, which contains a BS, an MF-RIS, randomly distributed users and a malicious E-Eve. Due to the existence of obstacles and sever attenuation, the direct links from the BS to users and the E-Eve are assumed to be totally blocked and communication links can only be established via the assistance of MF-RIS. To provide straightforward analyses, each node is equipped with a single antenna. The MF-RIS is composed of M reconfigurable elements embedded with active loads like delay lines and power amplifier [35]. For the sake of efficient resource utilization and high diversity gain, the MF-RIS operates under ES working mode. The amplitude coefficients for reflection and refraction are denoted as e_r and e_t , respectively, which satisfies the relationship $e_r + e_t = 1$ based on the conservation of energy. As a consequence, the superimposed signal is emitted from the BS to MF-RIS firstly, and then transmitted to reflection and refraction users simultaneously. In the considered MF-RIS-secured NOMA network, there exists a line-of-sight (LoS) link between the BS and MF-RIS [29]. The users are randomly located within a ring of radius R_d . Users located in the reflection space of the MF-RIS are termed as reflection users (u_r), while those situated on the opposite side are regarded as refraction users (u_t). Following the NOMA principle, we initially select one user, each from the reflection and refraction regions to form NOMA pairs. Subsequently, their signals are combined on the same subcarrier for non-orthogonal transmission with the assistance of MF-RIS, and at the receiver, the superimposed signals are extracted using SIC technology at the power domain level. Note that, in practical implementation, the radius of the MF-RIS service area is usually not large for establishing a stable

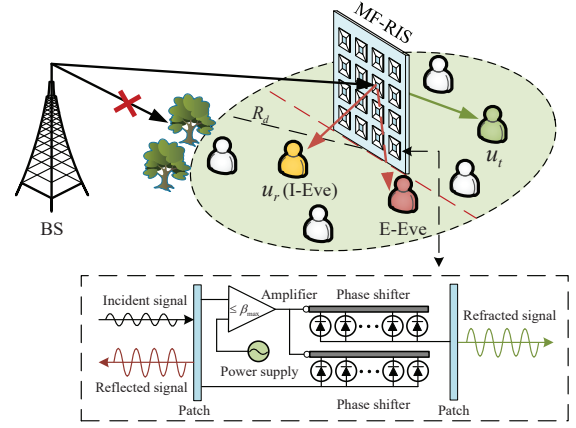


Fig. 1: An illustration of MF-RIS-secured NOMA networks.

LoS link and the path loss impact from the MF-RIS to users has little difference. Hence, the order of signal decoding when utilizing SIC technology primarily depends on the values of e_r and e_t [17]. The distances of u_r and u_t from the MF-RIS position are represented as d_r and d_t , respectively, and their probability density functions are given as

$$f_{d_\varphi}(x) = \frac{2}{\pi R_d^2} \cdot \frac{\partial}{\partial x} \int_0^\pi \int_0^x r dr d\theta = \frac{2x}{R_d^2}, \quad (1)$$

where $\varphi \in \{r, t\}$.

B. Channel Characteristics

The links from BS to MF-RIS and from MF-RIS to u_φ and E-Eve are denoted as \mathbf{H}_b , \mathbf{H}_φ , and \mathbf{H}_e , respectively. The complex channel gains are given as

$$\mathbf{H}_\eta = \sqrt{\chi d_\eta^{-\alpha}} \mathbf{h}_\eta = \sqrt{\chi d_\eta^{-\alpha}} [h_\eta^1, \dots, h_\eta^m, \dots, h_\eta^M]^H, \quad (2)$$

where \mathbf{H}_b and \mathbf{H}_φ are supposed to be Rician fading channels, $h_\eta^m = \sqrt{\frac{\kappa_\eta}{\kappa_\eta+1}} + \sqrt{\frac{1}{\kappa_\eta+1}} \tilde{h}_\eta^m$, $\tilde{h}_\eta^m \sim \mathcal{CN}(0, 1)$, $\eta \in \{b, r, t, e\}$, and $\varphi \in \{r, t\}$. The frequency dependent factor is denoted as χ . The terms d_b and d_e represent the distance from BS to MF-RIS and from MF-RIS to E-Eve, respectively. The term α is the path loss exponent. The Rician factor is given by κ_η and the Rician fading degenerates into Rayleigh fading by setting $\kappa_\eta = 0$. Furthermore, the malicious E-Eve cannot be served by the pre-designed beamforming from MF-RIS resulting in almost no strong LoS components in the signal received at E-Eve. Therefore, the links between MF-RIS and E-Eve are modeled as Rayleigh fading channels. We suppose that the perfect channel state information (CSI) of users can be obtained at BS by means of feedback or training processes, except for the E-Eve's since it hardly interacts with other nodes and often remains silent to avoid detection [41].

C. Signal Model

According to NOMA protocol, the superimposed signal is transmitted from BS to MF-RIS and then sent to users simultaneously. The signal received at u_φ can be given by

$$y_\varphi = \mathbf{H}_\varphi^H \Theta_\varphi \mathbf{H}_b \sum_{\tilde{\varphi} \in \{r, t\}} \sqrt{P_b a_{\tilde{\varphi}} x_{\tilde{\varphi}}} + \mathbf{H}_\varphi^H \Theta_\varphi \mathbf{n}_s + n, \quad (3)$$

where P_b denotes the transmit power at the BS and x_φ is the confidential signal of u_φ with unity power, i.e., $\mathbb{E}\{|x_\varphi|^2\} = 1$, $\varphi \in \{r, t\}$. To ensure user fairness, a_φ represents the power allocation factor of u_φ , which satisfies the relationship $a_r + a_t = 1$. In this paper, we suppose that u_r is the strong user with superior channel condition compared with u_t , and thus $a_t > a_r$. The diagonal matrix for u_φ is represented by $\Theta_\varphi = \text{diag}[\sqrt{\beta_\varphi^1} e^{j\theta_\varphi^1}, \dots, \sqrt{\beta_\varphi^m} e^{j\theta_\varphi^m}, \dots, \sqrt{\beta_\varphi^M} e^{j\theta_\varphi^M}]$, where β_φ^m indicates the amplification factor for u_φ of the m -th MF-RIS elements, $\beta_\varphi^m \in [0, \beta_{\max}]$ and $\beta_{\max} \geq 1$. In order to reduce the complexity of phase shift configuration, it is assumed that $\beta_\varphi^1 = \beta_\varphi^2 = \dots = \beta_\varphi^M = \beta_\varphi$, $\varphi \in \{r, t\}$ and $m = 1, 2, \dots, M$. In addition, $\mathbf{n}_s \sim \mathcal{CN}(\mathbf{0}, \sigma_s^2 \mathbf{1}_M)$ denotes the thermal noise caused by the active components at MF-RIS like asymmetric current mirrors and current-inverting converters, where $\mathbf{1}_M \in \mathbb{C}^{M \times 1}$ indicates the all-ones column vector [42]. The $n \sim \mathcal{CN}(0, \sigma_n^2)$ is the additive white Gaussian noise (AWGN) at the users with mean power parameter σ_n^2 .

Different from the passive RIS and STAR-RIS, the MF-RIS embeds a dedicated amplifier in each element to provide additional power gain to the incident signals, thereby further enhancing the reliability of LoS links. In this case, the total power consumed by MF-RIS-assisted NOMA networks can be represented as $P_{\text{tot}} = P_b + MP_r + 2M(P_{ps} + P_{dc})$, where P_b and P_r represent the transmit power at BS and the amplifier power at each element, P_{ps} and P_{dc} denote the power consumed by phase shifters and direct current biasing circuits [43], respectively.

Recall that the SIC decoding order mainly depends on the ES coefficients and u_r is supposed to be the strong user, we assume more energy is assigned to reflection region, i.e., $e_r \geq e_t$, which means u_r has better cascaded channel conditions than u_t . Accordingly, the SINR for u_r to decode u_t 's information can be given by

$$\gamma_{r,t} = \frac{P_b a_t \beta_r |\mathbf{H}_r^H \Phi_r \mathbf{H}_b|^2}{P_b a_r \beta_r |\mathbf{H}_r^H \Phi_r \mathbf{H}_b|^2 + \beta_r |\mathbf{H}_r^H \Phi_r \mathbf{n}_s|^2 + \sigma_n^2}, \quad (4)$$

where $\Phi_\varphi = \text{diag}[e^{j\theta_\varphi^1}, \dots, e^{j\theta_\varphi^m}, \dots, e^{j\theta_\varphi^M}]$. After removing u_t 's message, the SINR for u_r to decode its own information with imperfect SIC is shown as follows

$$\gamma_{r,r}^{\text{ipSIC}} = \frac{P_b a_r \beta_r |\mathbf{H}_r^H \Phi_r \mathbf{H}_b|^2}{\beta_r |\mathbf{H}_r^H \Phi_r \mathbf{n}_s|^2 + \varpi P_b |h_r^{\text{ip}}|^2 + \sigma_n^2}, \quad (5)$$

where $\varpi \in [0, 1]$ denotes the residual interference level for SIC. Specifically, $\varpi = 0$ and $\varpi \neq 0$ represent the switchover between perfect and imperfect SIC, respectively. Without loss of generality, the residual interference at u_φ generated by imperfect SIC is modeled as the Rayleigh random variable and the relative complex channel parameter is denoted by $h_\varphi^{\text{ip}} \sim \mathcal{CN}(0, \Omega_\varphi^{\text{ip}})$, $\varphi \in \{r, t\}$ [24].

Unlike the u_r who has superior channel condition, u_t will be allocated with a larger power coefficient by BS since it has inferior LoS link qualities, i.e., $a_t > a_r$. Thus, u_t can decode its own information directly from the superimposed signal without the assistance of SIC and the corresponding SINR can be given as

$$\gamma_{t,t} = \frac{P_b a_t \beta_t |\mathbf{H}_t^H \Phi_t \mathbf{H}_b|^2}{P_b a_r \beta_t |\mathbf{H}_t^H \Phi_t \mathbf{H}_b|^2 + \beta_t |\mathbf{H}_t^H \Phi_t \mathbf{n}_s|^2 + \sigma_n^2}. \quad (6)$$

D. Wiretapping Scenarios

Due to the open nature of wireless channels, signals are prone to interception by malicious Eves, leading to the leakage of users' private information. In order to further investigate the physical layer secrecy performance of the MF-RIS-assisted NOMA networks, we take into account two typical wiretapping cases, i.e., external and internal eavesdropping scenarios.

1) *External Wiretapping Scenario*: In the external wiretapping scenario, the Eve is not a legitimate registered user in the network, but can still receive the superimposed signals from the MF-RIS. In this paper, we deploy the E-Eve in the reflection area, which presents a challenging situation because more energy is split to the reflection signals by MF-RIS. The received signal at E-Eve is given by

$$y_{ee} = \mathbf{H}_e^H \Theta_r \mathbf{H}_b \sum_{\varphi \in \{r, t\}} \sqrt{P_b a_\varphi} x_\varphi + \mathbf{H}_e^H \Theta_r \mathbf{n}_s + n_e, \quad (7)$$

where $n_e \sim \mathcal{CN}(0, \sigma_e^2)$ indicates the AWGN at E-Eve with mean power parameter σ_e^2 .

Furthermore, the SINR for E-Eve to intercept u_t 's information can be given by

$$\gamma_{ee,t} = \frac{P_b a_t \beta_r |\mathbf{H}_e^H \Phi_r \mathbf{H}_b|^2}{P_b a_r \beta_r |\mathbf{H}_e^H \Phi_r \mathbf{H}_b|^2 + \beta_r |\mathbf{H}_e^H \Phi_r \mathbf{n}_s|^2 + \sigma_e^2}. \quad (8)$$

Similarly, the SINR for E-Eve to intercept u_r 's information with imperfect SIC can be given by

$$\gamma_{ee,r}^{\text{ipSIC}} = \frac{P_b a_r \beta_r |\mathbf{H}_e^H \Phi_r \mathbf{H}_b|^2}{\beta_r |\mathbf{H}_e^H \Phi_r \mathbf{n}_s|^2 + \varpi P_b |h_{e,r}^{\text{ip}}|^2 + \sigma_e^2}, \quad (9)$$

where $h_{e,r}^{\text{ip}} \sim \mathcal{CN}(0, \Omega_{e,r}^{\text{ip}})$ indicates the impact of residential interference brought by imperfect SIC on E-Eve.

2) *Internal Wiretapping Scenario*: Unlike the aforementioned external eavesdropping scenario, the I-Eve is a registered user within the NOMA service cell and can benefit from the cascaded channel gains brought by the MF-RIS [44]. For this scenario, we still consider a worst-case situation where u_r is identified as the I-Eve. Note that, to protect the signal privacy of u_t in the internal wiretapping scenario, the BS will adjust the power allocation of u_t so that a_t is less than a_r , ensuring that the signal of u_t is decoded last. Additionally, MF-RIS will also assign more energy to the refraction region to increase the secrecy capacity of u_t . As a consequence, the SINR for u_t to decode its own information and I-Eve to intercept u_t 's information with imperfect SIC can be given by

$$\gamma_{t,t}^{\text{ipSIC}} = \frac{P_b a_t \beta_t |\mathbf{H}_t^H \Phi_t \mathbf{H}_b|^2}{\varpi P_b |h_t^{\text{ip}}|^2 + \beta_t |\mathbf{H}_t^H \Phi_t \mathbf{n}_s|^2 + \sigma_n^2}, \quad (10)$$

and

$$\gamma_{ie,t}^{\text{ipSIC}} = \frac{P_b a_t \beta_r |\mathbf{H}_r^H \Phi_r \mathbf{H}_b|^2}{\beta_r |\mathbf{H}_r^H \Phi_r \mathbf{n}_s|^2 + \varpi P_b |h_{r,t}^{\text{ip}}|^2 + \sigma_e^2}, \quad (11)$$

respectively, where $h_{r,t}^{\text{ip}} \sim \mathcal{CN}(0, \Omega_{r,t}^{\text{ip}})$ represents the residential interference at I-Eve.

III. STATISTICAL PROPERTIES FOR CHANNELS

In this section, we investigate the secrecy performance of users in the MF-RIS-assisted NOMA networks. Specifically, we obtain the statistical characteristics of the legitimate and eavesdropping cascade channels to lay a foundation for the subsequent theoretical analysis of the user's SOP performance.

A. Statistical Properties for Legitimate Channels

Due to the independent phase-adjusting capability of each reconfigurable element, MF-RIS can attain coherent alignment between the incident channels and the reflection or refraction channels, leveraging user-specific CSI. As a consequence, the cascaded channels from BS to MF-RIS and then to u_φ can be defined as $\mathbf{H}_{b\varphi} = \mathbf{H}_\varphi^H \mathbf{\Theta}_\varphi \mathbf{H}_b = \Xi_{b\varphi} \sum_{m=1}^M |h_\varphi^m h_b^m|$, where the phase shifts at the m -th element $\theta_\varphi^m = \angle h_\varphi^m - \angle h_b^m$, $\Xi_{b\varphi} = \chi \sqrt{d_b^{-\alpha} d_\varphi^{-\alpha} \beta_\varphi}$, and $\sum_{m=1}^M |h_\varphi^m h_b^m|$ can be further defined as $\hat{\mathbf{H}}_{b\varphi}$, $\varphi \in \{r, t\}$. This capability serves to significantly enhance the cascaded channel gains. For the convenience of subsequent derivations, we provide the following lemma to describe the statistical characteristics of legitimate channels.

Lemma 1. *Upon utilizing the coherent phase-shifting scheme, the CDF and PDF of $|\hat{\mathbf{H}}_{b\varphi}|^2$ for u_φ can be given as*

$$F_{|\hat{\mathbf{H}}_{b\varphi}|^2}(x) = \frac{1}{\Gamma(k_\varphi)} \gamma\left(k_\varphi, \frac{\sqrt{x}}{l_\varphi}\right), \quad (12)$$

and

$$f_{|\hat{\mathbf{H}}_{b\varphi}|^2}(x) = \frac{x^{\frac{k_\varphi}{2}-1}}{2l_\varphi^{k_\varphi} \Gamma(k_\varphi)} e^{-\frac{\sqrt{x}}{l_\varphi}}, \quad (13)$$

where $\gamma(a, x) = \int_0^x p^{a-1} e^{-p} dp$ indicates the lower incomplete Gamma function [45, Eq. (8.350.1)] and $\Gamma(x) = \int_0^\infty e^{-p} p^{x-1} dp$ represents the Gamma function [45, Eq. (8.310.1)]. In addition, $k_\varphi = M[\mathbb{E}(|h_\varphi^m h_b^m|)]^2 / \mathbb{D}(|h_\varphi^m h_b^m|)$ and $l_\varphi = \mathbb{D}(|h_\varphi^m h_b^m|) / \mathbb{E}(|h_\varphi^m h_b^m|)$. The expectation and variance of single Rician cascaded channel are respectively given as

$$\mathbb{E}(|h_\varphi^m h_b^m|) = \frac{{}_1F_1(-\frac{1}{2}; 1; -\kappa_b) {}_1F_1(-\frac{1}{2}; 1; -\kappa_\varphi)}{4\pi^{-1} \sqrt{(\kappa_b + 1)(\kappa_\varphi + 1)}}, \quad (14)$$

and

$$\begin{aligned} \mathbb{D}(|h_\varphi^m h_b^m|) &= 1 - \frac{({}_1F_1(-\frac{1}{2}; 1; -\kappa_b))^2}{{}_1F_1(-\frac{1}{2}; 1; -\kappa_\varphi)} \\ &\quad \times \left(\pi {}_1F_1\left(-\frac{1}{2}; 1; -\kappa_\varphi\right) \right)^2, \end{aligned} \quad (15)$$

referring to [46]. ${}_1F_1(a; b; z) = \sum_{n=0}^\infty (a^{(n)} z^n) / (b^{(n)} n!)$ indicates the generalized hypergeometric series which is introduced from Kummer's function of the first kind [45, Eq. (9.14.1)].

Proof. Referring to [47], the approximated PDF expression of $\hat{\mathbf{H}}_{b\varphi}$ can be derived by utilizing Laguerre expansion as

$$f_{|\hat{\mathbf{H}}_{b\varphi}|}(x) = \frac{x^{k_\varphi-1}}{l_\varphi^{k_\varphi} \Gamma(k_\varphi)} e^{-\frac{x}{l_\varphi}}. \quad (16)$$

Furthermore, the expectation of $\hat{\mathbf{H}}_{b\varphi}$ is in accordance with $\mathbb{E}(|\hat{\mathbf{H}}_{b\varphi}|) = M\mathbb{E}(|h_\varphi^m h_b^m|)$ due to the linear characteristic of the expectation operation. Similar, since the cascaded Rician channels are assumed to be independent from each other, we can attain $\mathbb{D}(|\hat{\mathbf{H}}_{b\varphi}|) = M\mathbb{D}(|h_\varphi^m h_b^m|)$. On this basis, the PDF of $|\hat{\mathbf{H}}_{b\varphi}|^2$ is obtained as in (13). With the assistance of integral operation, the CDF expression of $|\hat{\mathbf{H}}_{b\varphi}|^2$ is further derived as (12), which completes the proof. \square

B. Statistical Properties for Eavesdropping Channels

Given that the E-Eve consistently maintains silence and avoids interacting with other network nodes, acquiring CSI for the eavesdropping channel becomes challenging for the BS. Consequently, we utilize statistical methods to evaluate the characteristics of the eavesdropping channels. Since the CSI of E-Eve is unavailable, we define that $\mathbf{H}_{be} = \mathbf{H}_e^H \mathbf{\Theta}_r \mathbf{H}_b = \Xi_{be} \sum_{m=1}^M |h_e^m h_b^m| e^{j\theta_{diff}^m}$, where $\Xi_{be} = \chi \sqrt{d_b^{-\alpha} d_e^{-\alpha} \beta_r}$. Considering the phase configuration of MF-RIS that has been completed based on the user's CSI, the phase difference is indicated as $\theta_{diff}^m = \angle h_b^m - \angle h_e^m$. In addition, the phases of h_b^m and h_e^m are also random variables following a uniform distribution, i.e., $\angle h_b^m, \angle h_e^m \sim U(0, 2\pi)$, $m = 1, 2, \dots, M$. In this case, the PDF of phase difference θ_{diff}^m is given by

$$f_{\theta_{diff}^m}(x) = \frac{1}{2\pi} \left(1 + \frac{x}{2\pi}\right), x \in [-2\pi, 0], \quad (17)$$

and

$$f_{\theta_{diff}^m}(x) = \frac{1}{2\pi} \left(1 - \frac{x}{2\pi}\right), x \in (0, 2\pi]. \quad (18)$$

Lemma 2. *The E-Eve is unable to achieve coherent matching of its own channels using MF-RIS, and thus the phase difference of the wiretapping cascade channels cannot be eliminated. In such a scenario, the CDF of $|\mathbf{H}_{be}|^2$ is given by*

$$F_{|\mathbf{H}_{be}|^2}(x) = 1 - e^{-vx}, \quad (19)$$

where $v = 2 / (M(\Xi_{be})^2)$.

Proof. With the assistance of Euler's formula, the real and imaginary component of cascaded wiretapping channels are denoted as $\text{Re}\{\mathbf{H}_{be}\} = \Xi_{be} \sum_{m=1}^M |h_e^m h_b^m| \cos \theta_{diff}^m$ and $\text{Im}\{\mathbf{H}_{be}\} = \Xi_{be} \sum_{m=1}^M |h_e^m h_b^m| \sin \theta_{diff}^m$, respectively. Since $\cos \theta_{diff}^m$ and $|h_e^m h_b^m|$ are both independent random variables, we can calculate the mean of $\cos \theta_{diff}^m$ as follows:

$$\mathbb{E}(\cos \theta_{diff}^m) = \int_{-2\pi}^0 \cos \theta_{diff}^m f_{\theta_{diff}^m}(\theta_{diff}^m) d\theta_{diff}^m. \quad (20)$$

Upon substituting (17) into (18), we can obtain $\mathbb{E}(\cos \theta_{diff}^m) = 0$. Similarly, we can further obtain

$$\mathbb{E}(\cos^2 \theta_{diff}^m) = \int_{-2\pi}^0 \cos^2 \theta_{diff}^m f_{\theta_{diff}^m}(\theta_{diff}^m) d\theta_{diff}^m = \frac{1}{4}. \quad (21)$$

Note that the identical conclusion can be reached for the case $\theta_{diff}^m \in (0, 2\pi]$. For the imaginary component, we have $\mathbb{E}(\sin \theta_{diff}^m) = 0$. On this basis, we suppose that $X = \Xi_{be} |h_e^m h_b^m|$ and $Y = \cos \theta_{diff}^m$. Hence, the variance value of $\Xi_{be} |h_e^m h_b^m| \cos \theta_{diff}^m$ is given by

$$\begin{aligned} \mathbb{D}(XY) &= \mathbb{D}(X) \mathbb{D}(Y) + \mathbb{D}(X) \mathbb{E}^2(Y) + \mathbb{E}^2(X) \mathbb{D}(Y) \\ &= (\Xi_{be})^2 / 4, \end{aligned} \quad (22)$$

where $\Xi_{be} = \chi \sqrt{d_b^{-\alpha} d_e^{-\alpha} \beta_r}$. Based on CLT, both $\text{Re}\{\mathbf{H}_{be}\}$ and $\text{Im}\{\mathbf{H}_{be}\}$ follow Gaussian distributions with a mean of zero and a variance of $M(\Xi_{be})^2 / 4$. As a consequence, the cascaded wiretapping channel \mathbf{H}_{be} can be regarded as the zero mean circle symmetric complex gaussian random variable, i.e., $\mathbf{H}_{be} \sim \mathcal{CN}(0, M(\Xi_{be})^2 / 2)$. In this case, $|\mathbf{H}_{be}|^2$ follows chi-square distribution of 2 degrees of freedom and the negative exponential distribution with the given CDF in (19). The proof is completed. \square

IV. SECRECY OUTAGE PROBABILITY ANALYSIS

In this section, the closed-form expressions of SOP for users in MF-RIS assisted NOMA networks are derived based on the channel statistical properties provided in Section III. To be specific, the users's secrecy outage behaviours are evaluated under external and internal wiretapping scenarios with the practical consideration of imperfect SIC process as well as thermal noise.

A. External Wiretapping Scenario

1) *SOP Expressions of u_r and u_t* : In the external wire-tapping scenario, the E-Eve is not registered in the MF-RIS service cell and often remains silent, meaning that the BS cannot obtain its CSI. After the E-Eve obtains the confidential signal, SIC technique is employed to decode users' private message step by step. Hence, we define the secrecy capacity of u_φ as $C_{ee,\varphi}^\varsigma = [\log(1 + \gamma_{\varphi,\varphi}^\varsigma) - \log(1 + \gamma_{ee,\varphi}^\varsigma)]^+$, where $\varphi \in \{r, t\}$ and $\varsigma \in \{\text{ipSIC}, \text{pSIC}\}$. Note that SIC is not adopted when u_r and E-Eve decode u_t 's information. Under this circumstance, the secrecy outage behaviours occur when $C_\varphi^\varsigma < R_\varphi$, and the SOP expressions are given in the following theorems.

Theorem 1. *In the external wiretapping scenario, the closed-form expressions of SOP for u_r with imperfect SIC in MF-RIS-assisted NOMA networks is given in (23) at the top of next page, where $\mu_{rr1} = \rho_e a_r \chi^2 \beta_r d_b^{-\alpha}$, $\mu_{rr2} = \varpi \rho_e$, $\mu_{rr3} = \beta_r \chi \sigma_s^2 M((M\kappa_r + 1)/(\kappa_r + 1))$, $\varepsilon_{er1} = P_b a_r \chi^2 \beta_r d_e^{-\alpha} d_b^{-\alpha}$, $\varepsilon_{er2} = \varpi P_b \Omega_{e,r}^{ip}$, $\varepsilon_{er3} = \beta_r \sigma_s^2 \chi d_e^{-\alpha} M((M\kappa_e + 1)/((\kappa_e + 1)\sigma_e^2)) + 1$, $q(z_w) = (z_w + 1)R_d/2$, $z_w = \cos((2w - 1)\pi/(2W))$ with $w = 1, 2, 3, \dots, W$, $\Lambda_r^{ip}(y) = 2^{R_r}(1 + \varepsilon_{er1}y/(\varepsilon_{er2} + \varepsilon_{er3})) - 1$ and we set $\rho_e = P_b/n_e$ indicating the SNR at the E-Eve. Moreover, $G_x = (X!)^2/(\tau_x(L'_X(\tau_x))^2)$ and τ_x represent the weight of Gauss-Laguerre quadrature formula and the x -th zero point of Laguerre polynomial $L_n(x) = \sum_{m=0}^n (-1)^m (n!x^m)/((n-m)!(m!)^2)$ with $x = 1, 2, 3, \dots, X$, respectively. X indicates a complexity accuracy tradeoff parameter and the equal sign in (23) can be established when X approaches infinity.*

Proof. Please refer to Appendix A. □

Corollary 1. *Conditioned on $\varpi = 0$, the closed-form SOP for u_r with perfect SIC in MF-RIS-assisted NOMA networks is given by*

$$P_r^{psic}(R_r) = \sum_{d=0}^D \sum_{w=1}^W \frac{G_d q(z_w) \sqrt{1 - z_w^2} \pi}{WR_d \Gamma(p_r)} \times \gamma \left(k_r, \sqrt{\frac{\mu_{rr3} + \sigma_n^2 (q(z_w))^\alpha}{l_r^2 \mu_{rr1} (\Lambda_r^p(M\tau_d))^{-1}}} \right), \quad (24)$$

where $\Lambda_r^p(y) = 2^{R_r}(1 + \varepsilon_{er1}y/\varepsilon_{er3}) - 1$.

Since the u_t is regarded as the weak user in the external wiretapping scenario, more power will be allocated to it by the BS to guarantee its first decoding order without the SIC process.

Theorem 2. *In the external wiretapping scenario, the closed-form SOP for u_t in MF-RIS-assisted NOMA networks is denoted as*

$$P_t(R_t) = \frac{\pi}{WR_d} \sum_{d=0}^D \sum_{w=1}^W \frac{G_d q(z_w) \sqrt{1 - z_w^2}}{\Gamma(p_t)} \times \gamma \left(k_t, \sqrt{\frac{(\mu_{tt3} + \sigma_n^2 (q(z_w))^\alpha) \Lambda_t(M\tau_d)}{l_t^2 (\mu_{tt1} - \mu_{tt2} \Lambda_t(M\tau_d))}} \right), \quad (25)$$

where $\mu_{tt1} = P_b a_t \chi^2 \beta_t d_b^{-\alpha}$, $\mu_{tt2} = P_b a_r \chi^2 \beta_t d_b^{-\alpha}$, $\mu_{tt3} = \beta_t \chi \sigma_s^2 M((M\kappa_t + 1)/(\kappa_t + 1))$, $\varepsilon_{et1} = \rho_e a_t \chi^2 \beta_r d_b^{-\alpha} d_e^{-\alpha}$, $\varepsilon_{et2} = \rho_e a_r \chi^2 \beta_r d_b^{-\alpha} d_e^{-\alpha}$, $\varepsilon_{et3} = (\beta_r \sigma_s^2 \chi d_e^{-\alpha} M((M\kappa_e + 1)/(\sigma_e^2 (\kappa_e + 1))) + 1)$, and $\Lambda_t(y) = 2^{R_t}(1 + \varepsilon_{et1}y/(\varepsilon_{et2}y + \varepsilon_{et3})) - 1$.

2) *Secrecy Diversity Order for u_r and u_t* : In order to accurately assess the anti-eavesdropping fading capability of the MF-RIS-assisted NOMA networks, we further derive asymptotic SOP expressions of u_t and u_r at the high SNR region. Based on this, we obtain the secrecy diversity order that characterizes the robustness of users in the external eavesdropping scenario.

Corollary 2. *When the transmitting SNR approaches infinity, the asymptotic SOP expression of u_r with imperfect SIC in MF-RIS-assisted NOMA networks is given by*

$$P_{ee,r,\infty}^{ipSIC}(R_r) = \sum_{s=0}^S \sum_{d=0}^D \sum_{w=1}^W \frac{\pi G_s G_d q(z_w) \sqrt{1 - z_w^2}}{WR_d \Gamma(p_r)} \times \gamma \left(k_r, \frac{1}{\hat{\mu}_{rr1}^2 l_r} \sqrt{\frac{\varpi \Omega_r^{ip} \tau_s \Lambda_r^{ip}(M\tau_d)}{(q(z_w))^{-\alpha}}} \right), \quad (26)$$

where $\hat{\mu}_{rr1} = a_r \chi^2 \beta_r d_b^{-\alpha}$.

Proof. When the transmitting SNR approaches infinity, the SINR for u_r to decode its own information with imperfect SIC can be recast as $\gamma_{r,r,\infty}^{ipSIC} = \frac{a_r \beta_r |\mathbf{H}_r^H \Phi_r \mathbf{H}_b|^2}{\varpi |\Omega_r^{ip}|^2}$. Upon replacing $\gamma_{r,r}^{ipSIC}$ with $\gamma_{r,r,\infty}^{ipSIC}$ and referring the remaining steps in Appendix A, (26) can be derived, and the proof is completed. □

Corollary 3. *When the transmitting SNR approaches infinity, the asymptotic SOP expression of u_r with perfect SIC in MF-RIS-assisted NOMA networks is given by (27) shown at the top of next page, where $\Xi_{r,\infty}^{pSIC} = 16(1 + \kappa_b)(1 + \kappa_r)/(3e^{\kappa_b + \kappa_r})$. The integral representation of hypergeometric functions is denoted as ${}_2F_1(\alpha, \beta; \gamma; z) = \frac{1}{B(\beta, \gamma - \beta)} \int_0^1 t^{\beta-1} (1-t)^{\gamma-\beta-1} (1-tz)^{-\alpha} dt$ [45, Eq. (9.111)] and $B(x, y) = 2 \int_0^1 t^{2x-1} (1-t^2)^{y-1} dt$ represents the beta function [45, Eq. (8.380.1)].*

Proof. Please refer to Appendix B. □

As for u_t , no SIC process is harnessed since it can decode its own signal directly. In this case, the asymptotic SOP expression of u_t is given in the following corollary.

$$P_{ee,r}^{ipSIC}(R_r) = \frac{\pi}{WR_d} \sum_{s=0}^S \sum_{d=0}^D \sum_{w=1}^W \frac{G_s G_d q(z_w)}{\Gamma(p_r)} \sqrt{1 - z_w^2} \gamma \left(k_r, \frac{1}{l_r} \sqrt{((\mu_{rr2} \Omega_r^{ip} \tau_s + \sigma_n^2) (q(z_w))^\alpha + \mu_{rr3}) \Lambda_r^{ip} (M\tau_d) / \mu_{rr1}} \right). \quad (23)$$

$$P_{ee,r,\infty}^{psic}(R_r) = \frac{\pi (\Xi_{r,\infty}^{pSIC})^M}{\mu_{rr1}^M WR_d (2M)!} \left({}_2F_1 \left(2, \frac{1}{2}; \frac{5}{2}; 1 \right) \right)^M \sum_{d=0}^D \sum_{w=1}^W G_d q(z_w) \sqrt{1 - z_w^2} ((\mu_{rr3} + \sigma_n^2 d^\alpha) \Lambda_r^p (M\tau_d))^M. \quad (27)$$

Corollary 4. For the case $a_t > \Lambda_t(M\tau_d) a_r$ and $a_t \leq \Lambda_t(M\tau_d) a_r$, the asymptotic SOP expressions of u_t in MF-RIS-assisted NOMA networks are respectively given by

$$P_{ee,t,\infty}(R_t) = \frac{\pi (\Xi_{t,\infty}^{pSIC})^M}{W (2M)! R_d} \left({}_2F_1 \left(2, \frac{1}{2}; \frac{5}{2}; 1 \right) \right)^M \times \sum_{d=0}^D \sum_{w=1}^W G_d q(z_w) \sqrt{1 - z_w^2} \times \left(\frac{(\mu_{tt3} + \sigma_n^2 (q(z_w))^\alpha) \Lambda_t(M\tau_d)}{\mu_{tt1} - \mu_{tt2} \Lambda_t(M\tau_d)} \right)^M, \quad (28)$$

and

$$P_{ee,t,\infty}(R_t) = 1, \quad (29)$$

where $\Xi_{t,\infty}^{pSIC} = 16(1 + \kappa_b)(1 + \kappa_t) / (3e^{\kappa_b + \kappa_t})$.

To gain more insights, the secrecy diversity order is adopted to evaluate the anti-eavesdropping fading characteristic of both users, which is defined as follows:

$$D_{ee,\varphi}^\varsigma = - \lim_{P_b \rightarrow \infty} \frac{\log(P_{ee,\varphi,\infty}^\varsigma)}{\log(P_b)}, \quad (30)$$

where $\varsigma \in \{\text{ipSIC}, \text{pSIC}\}$ and $\varphi \in \{r, t\}$. The $P_{ee,\varphi,\infty}^\varsigma$ can be obtained based on (26), (27), (28), and (29), respectively.

Remark 1. By substituting (27) and (28) into (30), the secrecy diversity orders of u_r with perfect SIC and u_t in the external wiretapping scenario are both equal to M , indicating that introducing more reconfigurable components in MF-RIS is beneficial for enhancing the anti-eavesdropping fading performance of the MF-RIS-assisted NOMA networks. Similarly, by substituting (26) into (30), we can obtain the secrecy diversity order of u_r with imperfect SIC, which equals zero. Although MF-RIS can support secure transmission in NOMA networks, the secrecy performance is still severely constrained by imperfect SIC in high SNR regions, leading to a noticeable error floor. Moreover, when the power budget of the proposed network is sufficient, it can be observed that the residual interference caused by imperfect SIC has a greater impact on network secrecy than the thermal noise generated by active devices. This phenomenon is also exhibited in Fig. 6.

B. Internal Wiretapping Scenario

1) *The SOP Expressions of u_t :* In the internal wiretapping scenario, the u_r is considered as an I-Eve, and it may attempt to eavesdrop on the signal of legitimate u_t . It is worth noting that the I-Eve is also a registered user in the MF-RIS service cell whose accurate CSI is known at the BS. Therefore, the

channel gain of the I-Eve can benefit from the precise beamforming provided by MF-RIS, leading to enhanced wiretapping performance. This also makes the internal eavesdropping scenario more challenging than the external scenario. The secrecy capacity of u_t in internal wiretapping scenario is denoted as $C_{ie,t}^\varsigma = [\log(1 + \gamma_{t,t}^\varsigma) - \log(1 + \gamma_{ie,t}^\varsigma)]^+$, where $\varsigma \in \{\text{ipSIC}, \text{pSIC}\}$ and the condition for the secrecy outage event to occur is $C_{ie,t}^\varsigma < R_t$. Hence, the SOP expressions are given in the following theorems.

Theorem 3. In the internal wiretapping scenario, the closed-form expression of SOP for u_t with imperfect SIC in MF-RIS-assisted NOMA networks is given in (31) shown at the top of next page, where $\mu_{rt1} = P_b a_t \chi^2 \beta_t d_b^{-\alpha}$, $\mu_{rt2} = \varpi P_b \Omega_t^{ip}$, $\mu_{rt3} = \beta_t \chi \sigma_s^2 M (M\kappa_t + 1) / (\kappa_t + 1)$, $\varepsilon_{rt1} = P_b a_t \chi^2 \beta_r d_b^{-\alpha}$, $\varepsilon_{rt2} = \varpi P_b \Omega_r^{ip}$, $\varepsilon_{rt3} = \beta_r \chi \sigma_s^2 M (M\kappa_r + 1) / (\kappa_r + 1)$, $h(x) = (x + 1) R_d^\alpha / 2$, $y_n = \cos((2n - 1)\pi / (2N))$, $z_i = \cos((2i - 1)\pi / (2I))$ with $n = 1, 2, 3, \dots, N$, $i = 1, 2, 3, \dots, I$, $\Psi(z) = 2^{R_t} (1 + \varepsilon_{rt1} \Omega_{br} / ((\varepsilon_{rt2} + \sigma_n^2) z + \varepsilon_{rt3})) - 1$, and $\Xi_{ie,t}^{ipSIC} = \pi^2 R_d^{2\alpha - 4} / (IN\alpha^2 \Gamma(k_t))$. Note that the closed-form expression of SOP for u_t with perfect SIC in MF-RIS-assisted NOMA networks can be attained by setting $\varpi = 0$ in (31).

Proof. Please refer to Appendix C. \square

2) *Secrecy Diversity Order for u_t :* In order to reap further insights, the asymptotic expressions of SOP for u_t with imperfect SIC under high SNR region is derived, which is shown in the following corollary.

Corollary 5. When the transmitting SNR approaches infinity, the asymptotic expression of SOP for u_t with imperfect SIC in MF-RIS-assisted NOMA networks is given by

$$P_{ie,t,\infty}^{ipSIC}(R_t) = \Xi_{ie,t}^{ipSIC} \sum_{i=1}^I \sum_{n=1}^N (h(y_n) h(z_i))^\frac{2}{\alpha} - 1 \times ((1 - y_n^2)(1 - z_i^2))^\frac{1}{2} \times \gamma \left(k_t, \frac{1}{l_t \hat{\mu}_{rt1}^2} \sqrt{\Upsilon(h(z_i)) \hat{\mu}_{rt2} h(y_n)} \right), \quad (32)$$

where $\hat{\mu}_{rt1} = a_t \chi^2 \beta_t d_b^{-\alpha}$, $\hat{\mu}_{rt2} = \varpi \Omega_t^{ip}$, $\hat{\varepsilon}_{rt1} = a_t \chi^2 \beta_r d_b^{-\alpha}$, $\hat{\varepsilon}_{rt2} = \varpi \Omega_r^{ip}$, and $\Upsilon(z) = 2^{R_t} (1 + \hat{\varepsilon}_{rt1} \Omega_{br} / (\hat{\varepsilon}_{rt2} z)) - 1$.

Corollary 6. When the transmitting SNR approaches infinity, the asymptotic expression of SOP for u_t with perfect SIC in

$$P_{ie,t}^{ipSIC}(R_t) = \Xi_{ie,t}^{ipSIC} \sum_{i=1}^I \sum_{n=1}^N (h(y_n) h(z_i))^{\frac{2}{\alpha}-1} \sqrt{(1-y_n^2)(1-z_i^2)} \gamma \left(k_t, \frac{\sqrt{\Psi(h(z_i))} ((\mu_{rt2} + \sigma_n^2) h(y_n) + \mu_{rt3})}{l_t \mu_{rt1}^2} \right). \quad (31)$$

MF-RIS-assisted NOMA networks is given by

$$P_{ie,t,\infty}^{pSIC}(R_t) = \frac{(\Xi_{t,\infty}^{pSIC})^M \pi^2 R_d^{2\alpha-4}}{N I \alpha^2 (2M)!} \left({}_2F_1 \left(2, \frac{1}{2}; \frac{5}{2}; 1 \right) \right)^M \times \sum_{i=1}^I \sum_{n=1}^N h(z_i)^{\frac{2}{\alpha}-1} (\Delta(h(z_i), h(y_n)))^M \times h(y_n)^{\frac{2}{\alpha}-1} \sqrt{(1-y_n^2)(1-z_i^2)}, \quad (33)$$

where $\Xi_{t,\infty}^{pSIC} = 16(1+\kappa_b)(1+\kappa_t)/(3e^{\kappa_b+\kappa_t})$ and $\Delta(z, y) = \Psi(z) (\sigma_n^2 y + \mu_{rt3}) / \mu_{rt1}$.

Remark 2. By substituting (32) and (33) into (30), the secrecy diversity order of u_t with imperfect and perfect SIC in the internal wiretapping scenario are both equal to zero. The reason is that cascaded channels of u_t and I-Eve can benefit from the beamforming gain provided by MF-RIS. Therefore, the secrecy diversity order of u_t is no longer dependent on the number of reconfigurable elements. This phenomenon is illustrated in Fig. 7, indicating that the internal wiretapping scenario poses a greater challenge for the MF-RIS-secured NOMA networks.

C. Secrecy Throughput Analysis

According to the aforementioned SOP performance, the delay-limited throughput of u_φ in MF-RIS-secured NOMA networks is defined as

$$\mathcal{T}_{\zeta,\varphi}^s(R_\varphi) = (1 - P_{\zeta,\varphi}^s(R_\varphi)) R_\varphi, \quad (34)$$

where $\zeta \in \{ee, ie\}$, $\varphi \in \{t, r\}$ and $\varsigma \in \{ipSIC, pSIC\}$ [12], [24]. $P_{\zeta,\varphi}^s(R_\varphi)$ can be attained from (23), (24), (25), and (31).

V. NUMERICAL RESULTS

In this section, numerical results are provided to verify the accuracy of the theoretical expressions derived in Section IV. Distinct secrecy insights of MF-RIS-assisted NOMA networks are also discussed in detail. Without otherwise stated, we set $\alpha = 2.2$, $\chi = -30$ dB [36]. The distance parameters are set to be $R_d = 20$ m, $d_b = 200$ m, and $d_e = 15$ m. The amplification factors at MF-RIS are $\beta_r = \beta_t = 10$ dB. Supposing that residual interference is approximately equivalent to 10% of the power of the decoded signal, the imperfect SIC parameter in external and internal wiretapping scenarios can be set as $\Omega_{r,t}^{ip} \approx -126.13$ dB, $\Omega_{e,r}^{ip} \approx -130.26$ dB, $\Omega_t^{ip} \approx -125.04$ dB and $\Omega_{r,t}^{ip} \approx -129.17$ dB, respectively [36]. The power setup of AWGN and thermal noise are given as $\sigma_n^2 = \sigma_e^2 = -90$ dBm and $\sigma_s^2 = -80$ dBm, respectively. In addition, the target secrecy rates for users $R_r = 0.1$ and $R_t = 0.05$ bit per channel use (BPCU) [41]. The power consumed by phase shifters and direct current biasing circuits are $P_{ps} = -10$ and $P_{dc} = -5$ dBm [43], respectively. To highlight the secrecy performance of the proposed network, the active RIS and STAR-RIS are both considered as benchmarks, which are defined as follows.

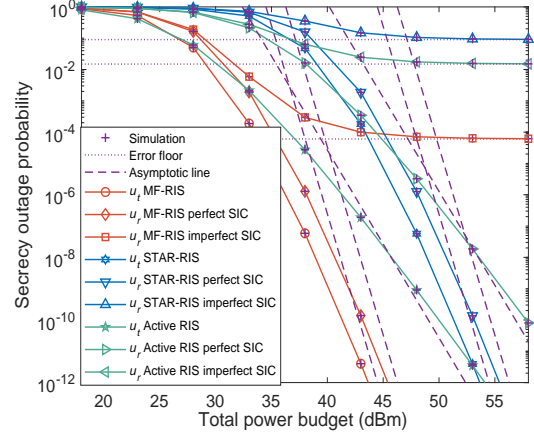


Fig. 2: The SOP performance versus the total power budget in the external wiretapping scenario, where $M = 12$, $e_r = 0.8$, $e_t = 0.2$, $a_r = 0.25$ and $a_t = 0.75$.

- 1) **Active RIS:** Active RIS allows $M/2$ reconfigurable elements to perform only reflection functions, while the other $M/2$ reconfigurable elements exclusively perform refraction functions, and all the elements can independently implement phase modulation. Additionally, active RIS has signal amplification capabilities and each reconfigurable element is equipped with a set of reflection or refraction power amplifiers. We suppose that the elements have identical amplification factors, i.e., $\beta_t^m = \beta_r^m$, $\beta_\varphi^1 = \beta_\varphi^2 = \dots = \beta_\varphi^{M/2}$ and $\varphi \in \{t, r\}$.
- 2) **STAR-RIS:** STAR-RIS can also perform dual-sided signal transmission, based on an ES strategy, simultaneously radiating the modulated signals to both the reflection and refraction regions. Unlike MF-RIS, STAR-RIS lacks signal amplification capabilities and does not include any active devices related to signal power amplification. In other words, STAR-RIS is almost passive. For a fair comparison, the ES coefficient for STAR-RIS is set to be the same as that for MF-RIS, i.e., $e_r = 0.8$ and $e_t = 0.2$.

A. External Wiretapping Scenario

Fig. 2 plots the SOP performance versus the system power budget in the external eavesdropping scenario. It is clear to see that the obtained analytical expressions are consistent with simulation results during the entire range of power budget, which validates the accuracy of analytical methods applied. Within the high SNR region, trends of the theoretical lines gradually converge with the asymptotic ones based on (26), (27) and (28) manifesting the validity of asymptotic theoretical expressions. Since the slopes of the asymptotic lines for MF-RIS and STAR-RIS are both greater than that of the active RIS,

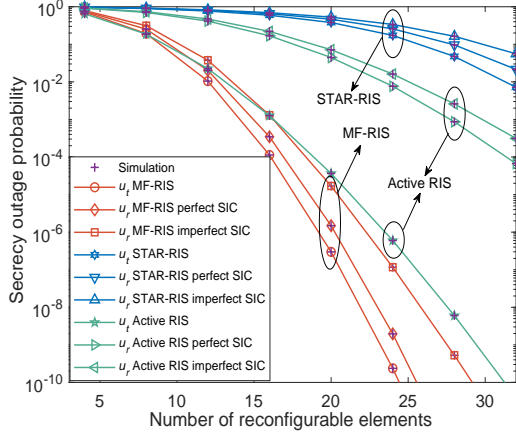


Fig. 3: The SOP performance versus the number of reconfigurable elements in the external wiretapping scenario, where $e_r = 0.8$, $e_t = 0.2$, $a_r = 0.3$ and $a_t = 0.7$.

this phenomenon also corroborates the analysis in Remark 1. From Fig. 2, we can observe that under the same system power constraints, the SOP performance of the proposed MF-RIS scheme significantly outperforms the STAR-RIS and active RIS alternatives. This is primarily due to the inherent advantages of MF-RIS, which encompass full-space coverage and signal amplification capabilities, capable of mitigating the adverse effects of multiplicative fading while enabling 360-degree wireless transmission. Additionally, Fig. 2 illustrates the impact of imperfect SIC on the physical layer secrecy for u_r . For active RIS, STAR-RIS and MF-RIS, the residual interference generated by imperfect SIC forces the SOP curves for u_r to converge to different error floors. This indicates that in the high SNR region, residual interference poses a more severe threat to users' privacy than thermal noise.

Fig. 3 plots the SOP performance versus the number of reconfigurable elements in the external eavesdropping scenario. Similar to Fig. 2, the numerical results align closely with the theoretical expressions. On the one hand, it can be observed that increasing the number of elements is advantageous in reducing the SOP for users in both the reflection and refraction regions. On the other hand, owing to MF-RIS's capability for independent bidirectional signal manipulation and amplification, it can achieve equivalent secrecy performance with the fewest reconfigurable elements compared to active RIS and STAR-RIS. Furthermore, we can note that the presence of imperfect SIC diminishes the performance gains obtained from MF-RIS elements. Therefore, devising appropriate SIC receivers to mitigate the impact of residual interference is crucial for enhancing the physical layer secrecy of MF-RIS-assisted NOMA networks.

Fig. 4 plots the system SOP performance versus the total power budget and the ES parameter in the external eavesdropping scenario. As the system power budget increases, the performance of the MF-RIS-assisted NOMA networks under perfect SIC improves steadily in terms of SOP. However, in the imperfect SIC case, the system SOP gradually converging

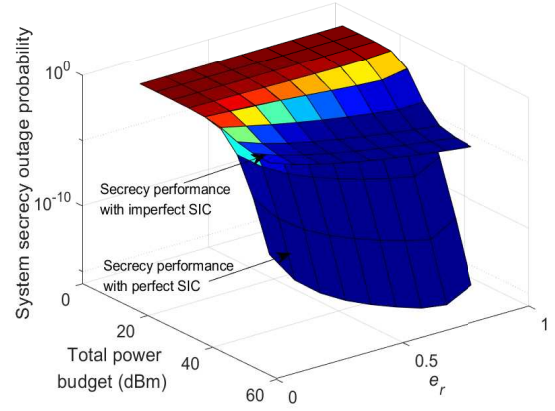


Fig. 4: The SOP performance versus the total power budget and ES coefficients in the external wiretapping scenario, where $M = 12$, $a_r = 0.25$ and $a_t = 0.75$.

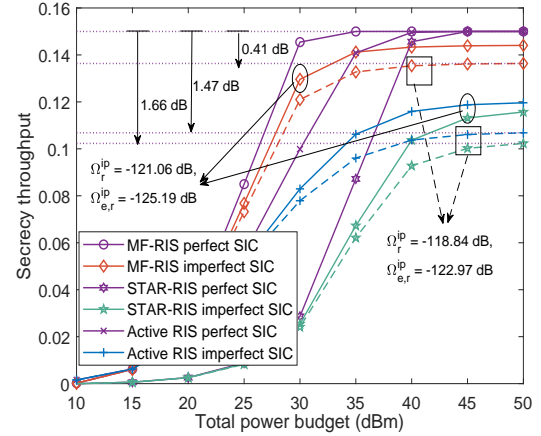


Fig. 5: The secrecy throughput performance versus the total power budget in the external eavesdropping scenario, where $M = 12$, $e_r = 0.8$, $e_t = 0.2$, $a_r = 0.25$ and $a_t = 0.75$.

to an error floor since the residual interference escalates with higher power budget. Furthermore, it is evident that when MF-RIS allocates more power to u_r (i.e., $e_r > 0.5$), the system secrecy outage behavior becomes better. However, when the e_r exceeds a certain threshold, the system's SOP increases instead of decreasing. This is because that an excessively large e_r leads to a reduction in the energy allocated to u_t , consequently diminishing the SINR when u_t decoding its own signal, ultimately compromising its secrecy capacity. This underscores the critical importance of selecting an appropriate ES strategy at the MF-RIS to safeguard NOMA networks.

Fig. 5 plots the system secrecy throughput versus the total power budget in the external eavesdropping scenario. From the figure, it can be observed that the delay-limited secrecy throughput of the MF-RIS is consistently higher than those of the benchmarks and eventually tends to stabilize with the increasing total power budget under perfect SIC case. This is because the SOP for users in the NOMA network

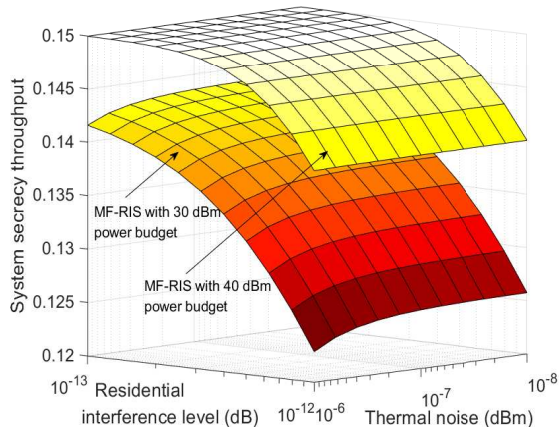


Fig. 6: The secrecy throughput performance versus the residential interference and thermal noise in the external wiretapping scenario, where $M = 12$, $e_r = 0.8$, $e_t = 0.2$, $a_r = 0.25$ and $a_t = 0.75$.

has already become sufficiently small within high power budget. The residual interference caused by imperfect SIC has the least impact on the proposed MF-RIS scheme, with a throughput loss of approximately 0.41 dB. In contrast, active RIS and STAR-RIS are more significantly affected by imperfect SIC, with throughput losses of up to 1.47 dB and 1.66 dB, respectively. This indicates that the MF-RIS demonstrates excellent robustness compared to the other two RIS configuration schemes.

Fig. 6 plots the system secrecy throughput versus the residential interference and thermal noise in the external eavesdropping scenario. This figure illustrates that increasing the total power budget can indeed enhance the overall secrecy throughput. When the total power budget is relatively abundant (40 dBm), the secrecy throughput of the MF-RIS-assisted NOMA networks is primarily influenced by the residual interference as the degree of imperfect SIC is directly proportional to the transmitting power of the BS. On the contrary, when the total power budget decreases (30 dBm), the secrecy throughput is jointly determined by the residual interference as well as the thermal noise. The phenomenon illustrated in Fig. 6 also answers the first and second questions that we raised in the introduction part.

B. Internal Wiretapping Scenario

Fig. 7 plots the SOP performance versus the total power budget in the internal eavesdropping scenario. From the figure, we can observe that the secrecy outage behavior for u_t in MF-RIS-assisted NOMA networks is superior to the other two benchmarks in both imperfect and perfect SIC cases. Furthermore, unlike the external eavesdropping scenario, the SOP for u_t eventually converges instead of continuing to decrease under perfect SIC conditions, and this phenomenon also corroborates the analyses in Remark 2. This is because the I-Eve's received SNR is proportional to the transmit power of BS. Therefore, as the total power budget increases, the

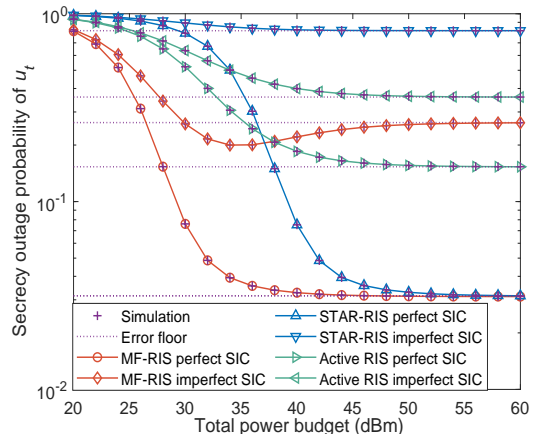


Fig. 7: The SOP performance versus the total power budget in the internal wiretapping scenario, where $M = 12$, $e_r = 0.2$, $e_t = 0.8$, $a_r = 0.9$ and $a_t = 0.1$.

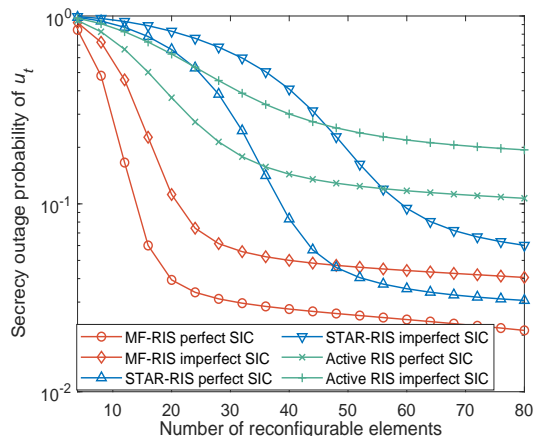


Fig. 8: The SOP performance versus the number of reconfigurable elements in the internal wiretapping scenario, where $e_r = 0.2$, $e_t = 0.8$, $a_r = 0.9$ and $a_t = 0.1$.

wiretapping capability of the I-Eve also improves. Moreover, it can be seen that under the imperfect SIC condition, the SOP for u_t initially decreases and then increases. This can be explained by the fact that in the high SNR region, the residual interference introduced by imperfect SIC is higher. At this point, the impact of residual interference on legitimate u_t is greater compared to its impact on I-Eve, leading to fluctuations in the SOP curve.

Fig. 8 plots the SOP performance versus the number of reconfigurable elements in the internal eavesdropping scenario. With the number of elements increases, the SOP of u_t gradually decreases, and the rate of decrease slows down. This is because, with a greater number of reconfigurable elements, the quality of cascaded eavesdropping channels for the I-Eve strengthens. In other words, both u_t and I-Eve can benefit from the beamforming gains from MF-RIS, which is evidently different from the external eavesdropping scenario illustrated in Fig. 3. Additionally, the figure indicates that MF-RIS

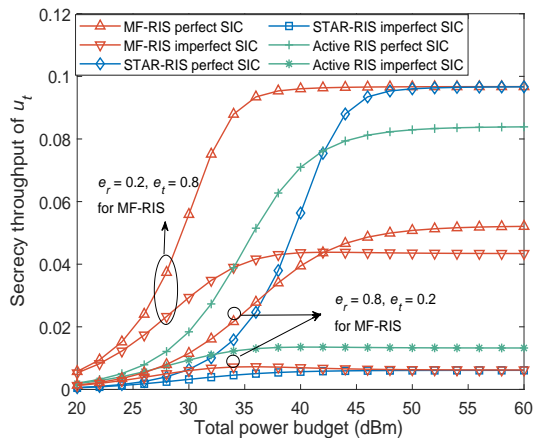


Fig. 9: The secrecy throughput performance versus the total power budget in the internal wiretapping scenario, where $a_r = 0.9$, $a_t = 0.1$ and $R_t = 0.1$ BPCU.

achieves the same level of secrecy performance as active RIS and STAR-RIS with only a small number of elements. This is attributed to the high diversity order and dual-sided signal amplification capability of MF-RIS. The SOP performances shown in Fig. 7 and Fig. 8 are remarkably different from that in the external wiretapping scenario, which also answers the last question proposed in the introduction part.

Fig. 9 plots the secrecy throughput versus the total power budget in the internal eavesdropping scenario. It can be seen from the figure that the secrecy throughput of u_t in the MF-RIS-assisted NOMA networks surpasses that of the other two benchmarks, mirroring the user's secrecy throughput performance in the external eavesdropping scenario, as illustrated in Fig. 5. It is noteworthy that the method to enhance the communication secrecy for the u_t involves deferring the decoding order of confidential information until it is the last one. Furthermore, MF-RIS should split more energy to u_t , specifically with $e_r = 0.2$ and $e_t = 0.8$. This ES strategy aims to diminish the SINR when the I-Eve decodes the confidential information, thereby augmenting the secrecy capacity of u_t . In cases where such assurance is unattainable, i.e., with $e_r = 0.8$ and $e_t = 0.2$, as evidenced in the figure, the secrecy throughput of u_t in the internal eavesdropping scenario experiences a notable degradation.

VI. CONCLUSION

In this paper, the physical layer secrecy of MF-RIS-assisted NOMA networks operating in ES mode was analyzed under both external and internal eavesdropping scenarios. We derived closed-form and approximate expressions of the SOP and secrecy throughput of randomly distributed users, and subsequently obtained the secrecy diversity orders in high SNR region. Theoretical analyses indicated that the secrecy diversity order of users is proportional to the number of reconfigurable elements only when the users are in the external eavesdropping scenario or ideal SIC case. Numerical results firstly demonstrate the superior secrecy performance of MF-

RIS-assisted NOMA networks compared to active RIS and STAR-RIS schemes. Secondly, residual interference caused by imperfect SIC poses a greater threat to the MF-RIS-secured NOMA networks with incremental total power budget. Finally, by redistributing the power allocation at BS and the ES coefficients at MF-RIS, the secrecy rates of users can be guaranteed in the internal wiretapping scenario.

APPENDIX A: PROOF OF LEMMA 1

In the external wiretapping scenario, the secrecy outage event of u_t occurs when $C_r^{ipSIC} = [\log(1 + \gamma_{r,r}^{ipSIC}) - \log(1 + \gamma_{ee,r}^{ipSIC})]^+ < R_r$. As a consequence, the SOP expression of u_t with imperfect SIC is denoted as

$$P_{ee,r}^{ipSIC} = \Pr\left(\log\left(1 + \gamma_{r,r}^{ipSIC}\right) - \log\left(1 + \gamma_{ee,r}^{ipSIC}\right)\right). \quad (\text{A.1})$$

Upon substituting (5) and (9) into (A.1), the SOP expression can be recast as

$$P_{ee,r}^{ipSIC} = \Pr\left(\frac{P_b a_r (\Xi_{br})^2 |\hat{\mathbf{H}}_{br}|^2}{\beta_r |\mathbf{H}_r^H \Phi_r \mathbf{n}_s|^2 + \varpi P_b |h_{ipu}|^2 + \sigma_n^2} < 2^{R_r} \times \left(1 + \frac{P_b a_r |\mathbf{H}_{be}|^2}{\beta_r |\mathbf{H}_e^H \Phi_r \mathbf{n}_s|^2 + \varpi P_b |h_{ipe}|^2 + \sigma_e^2}\right) - 1\right). \quad (\text{A.2})$$

Note that the thermal noise is $|\mathbf{H}_r^H \Phi_r \mathbf{n}_s|^2 = \chi d_r^{-\alpha} \sigma_s^2 \left|\sum_{m=1}^M h_r^m e^{j\theta_r^m}\right|^2$. To facilitate the calculation process, we define $\Delta_m = h_r^m e^{j\theta_r^m}$ and Δ_m is regarded as a novel complex Gaussian random variable which satisfies $\Delta_m \sim \mathcal{CN}(a, 2\sigma^2)$. In this case, the expectation as well as variance operation can be shown as

$$\mathbb{E}(|\Delta_m|^2) = \mathbb{D}(|\Delta_m|) + (\mathbb{E}(|\Delta_m|))^2, \quad (\text{A.3})$$

and

$$\begin{aligned} \mathbb{E}(|\Delta_m|^2) &= (M^2 \kappa_r / (\kappa_r + 1)) + (M / (\kappa_r + 1)) \\ &= M(M \kappa_r + 1) / (\kappa_r + 1), \end{aligned} \quad (\text{A.4})$$

respectively. Hence, the thermal noise received at u_r and E-Eve can be replaced with $M(M \kappa_r + 1) / (\kappa_r + 1)$ and $M(M \kappa_e + 1) / (\kappa_e + 1)$ and $M(M \kappa_e + 1) / (\kappa_e + 1)$. We further assume that $X = |\hat{\mathbf{H}}_{br}|^2$, $Y = |\mathbf{h}_e^H \Phi_r \mathbf{h}_b|^2$, $Z = d_r$ and $V = |h_{ipu}|^2$. The (A.2) can be derived as

$$P_{ee,r}^{ipSIC} = \int_0^\infty \int_0^\infty \int_0^{R_d} f_Z(z) f_V(v) f_Y(y) dy dv dz \times F_X\left(\frac{\Lambda_r^{ip}(y)}{\mu_{rr1}} (\mu_{rr2} v d_r^\alpha + \mu_{rr3} + \sigma_n^2 d_r^\alpha)\right). \quad (\text{A.5})$$

Defining $\Delta_1 = \int_0^{R_d} f_Z(z) F_X(\Lambda_r^{ip}(y) (\mu_{rr2} v d_r^\alpha + \mu_{rr3} + \sigma_n^2 d_r^\alpha) / \mu_{rr1})$ and substituting (1) into it, the Δ_1 can be rewritten with the assistance of Gauss-Chebyshev quadrature [48, Eq. (8.8.4)] as follows

$$\begin{aligned} \Delta_1 &= \frac{\pi}{\Gamma(k_r) W R_d} \sum_{w=1}^W q(z_w) \sqrt{1 - z_w^2} \\ &\times \gamma\left(k_r, \frac{\sqrt{(\mu_{rr2} v + \sigma_n^2) (q(z_w))^\alpha + \mu_{rr3}}}{l_r \sqrt{\mu_{rr1} (\Lambda_r^{ip}(y))^{-1}}}\right). \end{aligned} \quad (\text{A.6})$$

Considering $f_{|h_{\varphi}^{ip}|^2}(v) = (1/\Omega_{\varphi}^{ip}) e^{-v/\Omega_{\varphi}^{ip}}$ [12], the (A.5) can be rewritten as

$$P_{ee,r}^{ipSIC} = \frac{\pi}{MWR_d} \int_0^{\infty} f_V(v) dv \int_0^{\infty} e^{-\frac{1}{M}y} \Delta_1. \quad (\text{A.7})$$

By harnessing the Gauss-Laguerre quadrature formula and some straightforward calculations [48, Eq. (8.6.5)], the integral in (A.7) can be calculated to obtain (23), which completes the proof.

APPENDIX B: PROOF OF COROLLARY 3

To obtain the asymptotic SOP for u_r , it is pivotal to explore the statistical properties of $\hat{\mathbf{H}}_{b\varphi}$ when the transmit power approaches infinity. According to [45, Eq. (6.621.3)], the PDF of $|h_{\varphi}^m h_b^m|$ can be given in (B.1) via utilizing Laplace transform as shown at the top of this page, where $m = 1, 2, \dots, M$ and $\varphi \in \{t, r\}$. Under the condition that $P_b \rightarrow \infty$, the $s \rightarrow \infty$ and (B.1) can be simplified by keeping the first term of the series, i.e., $a = b = 0$. As a consequence, (B.1) is recast as

$$\mathcal{L}(f_{|h_{\varphi}^m h_b^m|}(x))(s) = {}_2F_1\left(2, \frac{1}{2}; \frac{5}{2}; 1\right) \frac{\Xi_{\varphi, \infty}^{pSIC}}{s^2}. \quad (\text{B.2})$$

Since $\hat{\mathbf{H}}_{b\varphi} = \sum_{m=1}^M |h_{\varphi}^m h_b^m|$, the PDF of $\hat{\mathbf{H}}_{b\varphi}$ can be attained by convolving the $f_{|h_{\varphi}^m h_b^m|}(x)$, $m = 1, 2, \dots, M$. Considering the convolution theorem, we have

$$\begin{aligned} \mathcal{L}(f_{\hat{\mathbf{H}}_{b\varphi}}(x))(s) &= \left(\mathcal{L}(f_{|h_{\varphi}^m h_b^m|}(x))(s)\right)^M \\ &= \left({}_2F_1\left(2, \frac{1}{2}; \frac{5}{2}; 1\right) \frac{\Xi_{\varphi, \infty}^{pSIC}}{s^2}\right)^M. \end{aligned} \quad (\text{B.3})$$

By taking the inverse Laplace transform of the above equation, we can further obtain the PDF of the cascaded channels $\hat{\mathbf{H}}_{b\varphi}$ given as follows

$$\begin{aligned} f_{\hat{\mathbf{H}}_{b\varphi}}(x) &= \mathcal{L}^{-1}\left(\left({}_2F_1\left(2, \frac{1}{2}; \frac{5}{2}; 1\right) \frac{\Xi_{\varphi, \infty}^{pSIC}}{s^2}\right)^M\right) \\ &= \frac{(16(1+\kappa_b)(1+\kappa_{\varphi})x)^M}{(2M)!(3e^{\kappa_b+\kappa_{\varphi}})^M}. \end{aligned} \quad (\text{B.4})$$

On this basis, the PDF of $|\hat{\mathbf{H}}_{b\varphi}|^2$ can be derived referring to the subsequence relationship

$$f_{|\hat{\mathbf{H}}_{b\varphi}|^2}(x) = \frac{1}{2\sqrt{x}} \left(f_{\hat{\mathbf{H}}_{b\varphi}}(\sqrt{x}) + f_{\hat{\mathbf{H}}_{b\varphi}}(-\sqrt{x})\right). \quad (\text{B.5})$$

The corresponding CDF of $|\hat{\mathbf{H}}_{b\varphi}|^2$ can be acquired by imposing derivation operation on (B.5). With following the similar procedure of (A.4)-(A.7) in Appendix A and replacing the original $F_X(\cdot)$ in (A.5), the asymptotic SOP expression of u_r with perfect SIC is derived as shown in (27). The proof is completed.

APPENDIX C: PROOF OF THEOREM 3

The proof starts with defining the secrecy outage event of u_r in the internal wiretapping scenario, which is shown as $P_{ie,t}^{ipSIC} = \Pr\left(\log\left(1 + \gamma_{t,t}^{ipSIC}\right) - \log\left(1 + \gamma_{ie,t}^{ipSIC}\right) < R_t\right)$. Upon substituting (6) and (4) into it and supposing that $X = |\hat{\mathbf{H}}_{bt}|^2$,

$V = |\hat{\mathbf{H}}_{br}|^2$, $Y = d_t^{\alpha}$ and $Z = d_r^{\alpha}$, $P_{ie,t}^{ipSIC}$ can be further rewritten as

$$\begin{aligned} P_{ie,t}^{ipSIC} &= \frac{l_r^{-k_r}}{2\Gamma(k_t)\Gamma(k_r)} \int_0^{R_d^{\alpha}} \int_0^{R_d^{\alpha}} f_Z(v) f_Y(v) dy dz \\ &\times \int_0^{\infty} v^{\frac{k_r}{2}-1} e^{-\frac{\sqrt{v}}{l_r}} \gamma\left(k_t, \frac{\sqrt{\Delta_2(z,v,y)}}{l_t}\right) dv, \end{aligned} \quad (\text{C.1})$$

where $\Delta_2(z, v, y) = \hat{\Psi}(z, v) (\mu_{rt3} + (\mu_{rt2} + \sigma_n^2) y) / \mu_{rt1}$ and $\hat{\Psi}(z, v) = 2^{R_t} \left(1 + \frac{\varepsilon_{rt1} v}{\varepsilon_{rt3} + (\varepsilon_{rt2} + \sigma_c^2) z}\right) - 1$. Due to the lack of accurate approximation method, the integral in (C.2) is hard to be tackled directly. For the purpose of tractability, the expectation operation is adopted to approximate the statistical properties of the cascaded internal wiretapping channels, which is shown as

$$\begin{aligned} \mathbb{E}\left(|\hat{\mathbf{H}}_{br}|^2\right) &= \mathbb{D}\left(|\hat{\mathbf{H}}_{br}|^2\right) + \left(\mathbb{E}\left(|\hat{\mathbf{H}}_{br}|^2\right)\right)^2 \\ &= M\mathbb{D}\left(|h_r^m h_b^m|\right) + (M\mathbb{E}\left(|h_r^m h_b^m|\right))^2, \end{aligned} \quad (\text{C.2})$$

where $\mathbb{E}\left(|h_r^m h_b^m|\right)$ and $\mathbb{D}\left(|h_r^m h_b^m|\right)$ are given in (14) and (15), respectively. They can also be expressed in the form of Bessel functions as follows:

$$\mathbb{E}\left(|h_r^m h_b^m|\right) = \frac{\pi e^{-\frac{1}{2}(\kappa_b + \kappa_r)}}{4\sqrt{(\kappa_b + 1)(\kappa_r + 1)}} \mathcal{I}_b \mathcal{I}_r, \quad (\text{C.3})$$

and

$$\mathbb{D}\left(|h_r^m h_b^m|\right) = 1 - \frac{\pi^2 e^{-(\kappa_b + \kappa_r)} \mathcal{I}_b^2 \mathcal{I}_r^2}{16(\kappa_b + 1)(\kappa_r + 1)}, \quad (\text{C.4})$$

where $\mathcal{I}_b = (\kappa_b + 1) I_0\left(\frac{\kappa_b}{2}\right) + \kappa_b I_1\left(\frac{\kappa_b}{2}\right)$ and $\mathcal{I}_r = (\kappa_r + 1) I_0\left(\frac{\kappa_r}{2}\right) + \kappa_r I_1\left(\frac{\kappa_r}{2}\right)$ and $I_\nu(\cdot)$ indicates the modified ν -order Bessel function of the first kind [45, Eq. (8.431)].

Hence, the expectation of $|\hat{\mathbf{H}}_{br}|^2$ is given by

$$\begin{aligned} \Omega_{br} &= M \left(1 - \frac{\pi^2 e^{-(\kappa_b + \kappa_r)} \mathcal{I}_b^2 \mathcal{I}_r^2}{16(\kappa_b + 1)(\kappa_r + 1)}\right) \\ &+ \left(\frac{M\pi e^{-\frac{1}{2}(\kappa_b + \kappa_r)}}{4\sqrt{(\kappa_b + 1)(\kappa_r + 1)}} \mathcal{I}_b \mathcal{I}_r\right)^2. \end{aligned} \quad (\text{C.5})$$

By substituting (C.5) into (C.1), we have $P_{ie,t}^{ipSIC}(R_t) = \int_0^{R_d^{\alpha}} \int_0^{R_d^{\alpha}} f_Z(v) f_Y(v) F_X\left(\frac{\hat{\Psi}(z)(\mu_{rt3} + (\mu_{rt2} + \sigma_n^2)y)}{\mu_{rt1}}\right) dy dz$

and $\hat{\Psi}(z) = 2^{R_t} \left(1 + \frac{\varepsilon_{rt1} \Omega_{br}}{\varepsilon_{rt3} + (\varepsilon_{rt2} + \sigma_c^2) z}\right) - 1$. Referring to the procedure illustrated in (A.2)-(A.7) and applying some simple calculations, we can obtain (31). The proof is completed.

REFERENCES

- [1] Z. Zhang, Y. Xiao, Z. Ma, M. Xiao, Z. Ding, X. Lei, G. K. Karagiannidis, and P. Fan, "6G wireless networks: Vision, requirements, architecture, and key technologies," *IEEE Veh. Technol. Mag.*, vol. 14, no. 3, pp. 28–41, Sep. 2019.
- [2] X. You, C.-X. Wang, J. Huang, X. Gao, Z. Zhang, M. Wang, Y. Huang, C. Zhang, Y. Jiang, J. Wang *et al.*, "Towards 6G wireless communication networks: Vision, enabling technologies, and new paradigm shifts," *Sci. China Inf. Sci.*, vol. 64, no. 1, pp. 1–74, 2021.
- [3] W. Saad, M. Bennis, and M. Chen, "A vision of 6G wireless systems: Applications, trends, technologies, and open research problems," *IEEE Netw.*, vol. 34, no. 3, pp. 134–142, May 2020.
- [4] Q. Wu and R. Zhang, "Towards smart and reconfigurable environment: Intelligent reflecting surface aided wireless network," *IEEE Commun. Mag.*, vol. 58, no. 1, pp. 106–112, Jan. 2020.

$$\mathcal{L}\left(f_{|h_{\varphi}^m h_b^m|}(x)\right)(s) = \sum_{a=0}^{\infty} \sum_{b=0}^{\infty} \frac{(\kappa_b \kappa_{\varphi})^a ((1 + \kappa_b)(1 + \kappa_{\varphi}))^{(a+1)}}{4^{b-a-1} \pi^{-\frac{1}{2}} ((a!) (b!))^2 e^{\kappa_b + \kappa_{\varphi}}} \times {}_2F_1\left(2(a+1), \frac{1}{2} + a - b; \frac{5}{2} + a + b; \frac{s - 2\sqrt{(1 + \kappa_b)(1 + \kappa_{\varphi})}}{s + 2\sqrt{(1 + \kappa_b)(1 + \kappa_{\varphi})}}\right) \Gamma\left(2(b+1), 2(a+1), a + b + \frac{5}{2}\right) \quad (\text{B.1})$$

- [5] S. Gong, X. Lu, D. T. Hoang, D. Niyato, L. Shu, D. I. Kim, and Y.-C. Liang, "Toward smart wireless communications via intelligent reflecting surfaces: A contemporary survey," *IEEE Commun. Surveys Tutorials*, vol. 22, no. 4, pp. 2283–2314, Jun 2020.
- [6] Q. Wu, S. Zhang, B. Zheng, C. You, and R. Zhang, "Intelligent reflecting surface-aided wireless communications: A tutorial," *IEEE Trans. Commun.*, vol. 69, no. 5, pp. 3313–3351, May 2021.
- [7] Y. Yang, B. Zheng, S. Zhang, and R. Zhang, "Intelligent reflecting surface meets OFDM: Protocol design and rate maximization," *IEEE Trans. Commun.*, vol. 68, no. 7, pp. 4522–4535, Jul. 2020.
- [8] L. Yang, Y. Yang, M. O. Hasna, and M.-S. Alouini, "Coverage, probability of SNR gain, and DOR analysis of RIS-aided communication systems," *IEEE Wireless Commun. Lett.*, vol. 9, no. 8, pp. 1268–1272, Aug. 2020.
- [9] J. Hu, H. Zhang, B. Di, L. Li, K. Bian, L. Song, Y. Li, Z. Han, and H. V. Poor, "Reconfigurable intelligent surface based RF sensing: Design, optimization, and implementation," *IEEE J. Sel. Areas Commun.*, vol. 38, no. 11, pp. 2700–2716, Nov. 2020.
- [10] X. Wang, Z. Fei, J. Huang, and H. Yu, "Joint waveform and discrete phase shift design for RIS-assisted integrated sensing and communication system under Cramer-Rao bound constraint," *IEEE Trans. Veh. Technol.*, vol. 71, no. 1, pp. 1004–1009, Jan. 2022.
- [11] G. Sun, X. Tao, N. Li, and J. Xu, "Intelligent reflecting surface and UAV assisted secrecy communication in millimeter-wave networks," *IEEE Trans. Veh. Technol.*, vol. 70, no. 11, pp. 11 949–11 961, Nov. 2021.
- [12] Y. Pei, X. Yue, W. Yi, Y. Liu, X. Li, and Z. Ding, "Secrecy outage probability analysis for downlink RIS-NOMA networks with on-off control," *IEEE Trans. Veh. Technol.*, vol. 72, no. 9, pp. 11 772–11 786, Sep. 2023.
- [13] W. Khalid, M. A. U. Rehman, T. Van Chien, Z. Kaleem, H. Lee, and H. Yu, "Reconfigurable intelligent surface for physical layer security in 6G-IoT: Designs, issues, and advances," *IEEE Internet Things J.*, vol. 11, no. 2, pp. 3599–3613, Jan. 2024.
- [14] L. Dai, B. Wang, M. Wang, X. Yang, J. Tan, S. Bi, S. Xu, F. Yang, Z. Chen, M. D. Renzo, C.-B. Chae, and L. Hanzo, "Reconfigurable intelligent surface-based wireless communications: Antenna design, prototyping, and experimental results," *IEEE Access*, vol. 8, pp. 45 913–45 923, Mar. 2020.
- [15] Y. Liu, X. Mu, J. Xu, R. Schober, Y. Hao, H. V. Poor, and L. Hanzo, "STAR: Simultaneous transmission and reflection for 360° coverage by intelligent surfaces," *IEEE Wireless Commun.*, vol. 28, no. 6, pp. 102–109, Dec. 2021.
- [16] J. Xu, Y. Liu, X. Mu, and O. A. Dobre, "STAR-RISs: Simultaneous transmitting and reflecting reconfigurable intelligent surfaces," *IEEE Commun. Lett.*, vol. 25, no. 9, pp. 3134–3138, Sep. 2021.
- [17] C. Zhang, W. Yi, Y. Liu, Z. Ding, and L. Song, "STAR-IOs aided NOMA networks: Channel model approximation and performance analysis," *IEEE Trans. Wireless Commun.*, vol. 21, no. 9, pp. 6861–6876, Sep. 2022.
- [18] A. Papazafeiropoulos, Z. Abdullah, P. Kourtessis, S. Kisseleff, and I. Krikidis, "Coverage probability of STAR-RIS-assisted massive MIMO systems with correlation and phase errors," *IEEE Wireless Commun. Lett.*, vol. 11, no. 8, pp. 1738–1742, Aug. 2022.
- [19] H. Niu, Z. Chu, F. Zhou, and Z. Zhu, "Simultaneous transmission and reflection reconfigurable intelligent surface assisted secrecy MISO networks," *IEEE Commun. Lett.*, vol. 25, no. 11, pp. 3498–3502, Nov. 2021.
- [20] G. Hu, Z. Li, J. Si, K. Xu, Y. Cai, D. Xu, and N. Al-Dhahir, "Analysis and optimization of STAR-RIS-assisted proactive eavesdropping with statistical CSI," *IEEE Trans. Veh. Technol.*, vol. 72, no. 5, pp. 6850–6855, May 2023.
- [21] M. Ahmed, A. Wahid, S. S. Laique, W. U. Khan, A. Ihsan, F. Xu, S. Chatzinotas, and Z. Han, "A survey on STAR-RIS: Use cases, recent advances, and future research challenges," *IEEE Internet Things J.*, vol. 10, no. 16, pp. 14 689–14 711, Aug. 2023.
- [22] X. Pei, Y. Chen, M. Wen, H. Yu, E. Panayirci, and H. V. Poor, "Next-generation multiple access based on NOMA with power level modulation," *IEEE J. Sel. Areas Commun.*, vol. 40, no. 4, pp. 1072–1083, Apr. 2022.
- [23] B. Zhao, C. Zhang, W. Yi, and Y. Liu, "Ergodic rate analysis of STAR-RIS aided NOMA systems," *IEEE Commun. Lett.*, vol. 26, no. 10, pp. 189–204, Apr. 2022.
- [24] X. Yue, J. Xie, Y. Liu, Z. Han, R. Liu, and Z. Ding, "Simultaneously transmitting and reflecting reconfigurable intelligent surface assisted NOMA networks," *IEEE Trans. Wireless Commun.*, vol. 22, no. 1, pp. 189–204, Jan. 2023.
- [25] F. Karim, S. K. Singh, K. Singh, S. Prakriya, and M. F. Flanagan, "On the performance of STAR-RIS-aided NOMA at finite blocklength," *IEEE Wireless Commun. Lett.*, vol. 12, no. 5, pp. 868–872, May 2023.
- [26] B. Y. D. Rito and K. H. Li, "SER-effective constellation scaling and rotation in STAR-RIS-assisted uplink NOMA," *IEEE Commun. Lett.*, vol. 27, no. 9, pp. 2506–2510, Sep. 2023.
- [27] X. Yu, K. Shen, and X. Dang, "Secure performance of STAR-RIS aided NOMA system with imperfect SIC," *IEEE Wireless Commun. Lett.*, vol. 12, no. 12, pp. 2023–2027, Dec. 2023.
- [28] X. Li, Y. Zheng, M. Zeng, Y. Liu, and O. A. Dobre, "Enhancing secrecy performance for STAR-RIS NOMA networks," *IEEE Trans. Veh. Technol.*, vol. 72, no. 2, pp. 2684–2688, Feb. 2022.
- [29] Y. Han, N. Li, Y. Liu, T. Zhang, and X. Tao, "Artificial noise aided secure NOMA communications in STAR-RIS networks," *IEEE Wireless Commun. Lett.*, vol. 11, no. 6, pp. 1191–1195, Jun. 2022.
- [30] H. Han, Y. Cao, N. Deng, C. Xing, N. Zhao, Y. Li, and X. Wang, "Secure transmission for STAR-RIS aided NOMA against internal eavesdropping," *IEEE Trans. Veh. Technol.*, vol. 72, no. 11, pp. 15 068–15 073, Nov. 2023.
- [31] Z. Zhang, J. Chen, Y. Liu, Q. Wu, B. He, and L. Yang, "On the secrecy design of STAR-RIS assisted uplink NOMA networks," *IEEE Trans. Wireless Commun.*, vol. 21, no. 12, pp. 11 207–11 221, Dec. 2022.
- [32] Y. Zhang, Z. Yang, J. Cui, P. Xu, G. Chen, Y. Wu, and M. D. Renzo, "STAR-RIS assisted secure transmission for downlink multi-carrier NOMA networks," *IEEE Trans. Inf. Forensics Security*, vol. 18, pp. 5788–5803, Sep. 2023.
- [33] Z. Zhang, L. Dai, X. Chen, C. Liu, F. Yang, R. Schober, and H. V. Poor, "Active RIS vs. passive RIS: Which will prevail in 6G?" *IEEE Trans. Commun.*, vol. 71, no. 3, pp. 1707–1725, Mar. 2023.
- [34] J. Xu, J. Zuo, J. T. Zhou, and Y. Liu, "Active simultaneously transmitting and reflecting (STAR)-RISs: Modeling and analysis," *IEEE Commun. Lett.*, vol. 27, no. 9, pp. 2466–2470, Sep. 2023.
- [35] W. Wang, W. Ni, and H. Tian, "Multi-functional RIS-aided wireless communications," *IEEE Internet Things J.*, vol. 10, no. 23, pp. 21 133–21 134, Dec. 2023.
- [36] X. Yue, J. Xie, C. Ouyang, Y. Liu, X. Shen, and Z. Ding, "Active simultaneously transmitting and reflecting surface assisted NOMA networks," *IEEE Trans. Wireless Commun.*, to appear in 2024.
- [37] A. Zheng, W. Ni, W. Wang, H. Tian, Y. C. Eldar, and D. Niyato, "Multi-functional RIS: Signal modeling and optimization," *IEEE Trans. Veh. Technol.*, pp. 1–5, to appear in 2024 2023.
- [38] Y. Yan, Y. Wang, W. Ni, and D. Niyato, "Joint beamforming design for multi-functional RIS-aided uplink communications," *IEEE Commun. Lett.*, vol. 27, no. 10, pp. 2697–2701, Oct. 2023.
- [39] A. Zheng, W. Ni, W. Wang, and H. Tian, "Next-generation RIS: From single to multiple functions," *IEEE Wireless Commun. Lett.*, vol. 12, no. 12, pp. 1988–1992, Dec. 2023.
- [40] A. Papazafeiropoulos, H. Ge, P. Kourtessis, T. Ratnarajah, S. Chatzinotas, and S. Papavassiliou, "Two-timescale design for active STAR-RIS aided massive MIMO systems," *IEEE Trans. Veh. Technol.*, to appear in 2024 2024.
- [41] X. Li, Y. Pei, X. Yue, Y. Liu, and Z. Ding, "Secure communication of active RIS assisted NOMA networks," *IEEE Trans. Wireless Commun.*, to appear in 2024 2023.

- [42] K. Liu, Z. Zhang, L. Dai, S. Xu, and F. Yang, "Active reconfigurable intelligent surface: Fully-connected or sub-connected?" *IEEE Commun. Lett.*, vol. 26, no. 1, pp. 167–171, Jan. 2022.
- [43] K. Zhi, C. Pan, H. Ren, K. K. Chai, and M. ElKashlan, "Active RIS versus passive RIS: Which is superior with the same power budget?" *IEEE Commun. Lett.*, vol. 26, no. 5, pp. 1150–1154, May 2022.
- [44] N. Li, M. Li, Y. Liu, C. Yuan, and X. Tao, "Intelligent reflecting surface assisted NOMA with heterogeneous internal secrecy requirements," *IEEE Wireless Commun. Lett.*, vol. 10, no. 5, pp. 1103–1107, May 2021.
- [45] I. Gradshteyn and I. M. Ryzhik, "Table of integrals, series, and products, 6th ed," 2000.
- [46] M. K. Simon, *Probability distributions involving Gaussian random variables: A handbook for engineers and scientists*. Springer, 2002.
- [47] S. Primak, V. Kontorovich, and V. Lyandres, *Stochastic methods and their applications to communications: stochastic differential equations approach*. John Wiley & Sons, 2005.
- [48] F. B. Hildebrand, *Introduction to numerical analysis*. Courier Corporation, 1987.